JSS Focus Issue on Printable Functional Materials for Electronics and Energy Applications

Ultrafast Atmospheric-Pressure-Plasma-Jet Sintering of Nanoporous TiO_2-SnO_2 Composites with Features Defined by Screen-Printing

Ching Wang,[a] I-Chun Cheng,[b,c,z] and Jian-Zhang Chen[a,z]

[a]*Graduate Institute of Applied Mechanics, National Taiwan University, Taipei City 10617, Taiwan*
[b]*Graduate Institute of Photonics and Optoelectronics, National Taiwan University, Taipei City 10617, Taiwan*
[c]*Department of Electrical Engineering, National Taiwan University, Taipei City 10617, Taiwan*

We investigated atmospheric-pressure-plasma-jet (APPJ)-sintered nanoporous TiO_2 and TiO_2-SnO_2 composites with patterns defined by the screen-printing technique. The pastes used for screen-printing were made of oxide nanoparticles and organic binders. After using screen-printing to define the features, APPJ was then used to rapidly sinter the screen-printed pastes. APPJ sintering for 30 s can efficiently remove the organic compounds and sinter the nanoparticles, with transmittance haze values comparable to those of nanoporous oxides prepared by conventional furnace calcination. Dye-sensitized solar cells with APPJ-sintered photoanodes (sintering time $\geq$1 min) showed efficiencies comparable to or exceeding those of cells prepared by conventional furnace calcination.
 [DOI: 10.1149/2.0041504jss]

Manuscript submitted December 15, 2014; revised manuscript received January 20, 2015. Published January 29, 2015. *This paper is part of the JSS Focus Issue on Printable Functional Materials for Electronics and Energy Applications.*

Screen-printing is a mature scalable low-cost deposition process that has been extensively used for the fabrication of various types of devices.[1–8] In industry, this technique is commonly used in roll-to-roll processes in which printing is performed when the web is stationary. Because alignment can be more easily achieved in this technique, it is customarily used in printing the second and follow-up layers.[9,10] Recently, screen-printing has attracted renewed interest owing to the search for low-cost fabrication processes for flexible/stretchable supercapacitors,[3,4] lithium ion batteries,[4] flexible/stretchable organic thin film transistors,[11–13] light emitting diodes,[12–14] flexible carbon nanotube thin film transistors,[10] thermoelectric modules,[1] RFIDs,[7] and dye-sensitized solar cells (DSSCs).[2,15–20]

We have applied the screen-printing technique to produce ceramic-type metal oxides. Screen-printing administers the pastes containing the desired oxide nanoparticles with organic solvents or binders to maintain the required viscosity. The removal of these organic compounds usually requires calcination or annealing processes that are time-consuming and require a high thermal budget. In our previous study, we have developed a rapid atmospheric-pressure-plasma-jet (APPJ) sintering process for nanoporous TiO_2 with a sintering time as short as 1 min. The sintering time can be further reduced to 30 s by introducing air-quenching to increase the oxidization ability.[21–23] In contrast, furnace calcination would require ~15 min excluding the temperature ramping and cooling times. This ultrafast sintering process was made possible by the synergistic effect of highly reactive/active N_2 plasmas and heat generated in APPJs.[21,22] Most recently, we further used this sequential screen-printing and APPJ-sintering process for the fabrication of reduced graphene oxide (rGO) counter electrodes of DSSCs. The processing time was only 11 s owing to the vigorous reaction between the N_2 APPJ and the carbon-based materials; in comparison, conventional furnace calcination would take 15 min at 400°C. The estimated energy consumption per unit processing area is less than one-third that of the conventional furnace calcination process.[19]

In this paper, we describe the sequential screen-printing and APPJ-sintering processes, as well as the preparation procedure of the oxide nanoparticle pastes in detail. Nanoporous TiO_2 and TiO_2-SnO_2 composites are sintered by APPJs and characterized. The synthesized nanoporous oxides are implemented as the photoanodes of DSSCs for functionality testing.

[z]E-mail: jchen@ntu.edu.tw; iccheng@ntu.edu.tw

Experimental

Details of APPJ operation.— The schematic of the APPJ apparatus is shown in Figure 1a. A quartz tube of 2-cm length and 3-cm inside diameter is installed downstream of the plasma. The APPJ operation conditions are nitrogen gas flow of 30 slm, applied voltage of 275 V, and on/off duty cycle of 7/33 μs. The distance between the nozzle exit of the plasma jet and the stage was 2 cm, and the gap between the stage and the glass tube exit was 1 mm. The surface temperature evolution for APPJ treatment is shown in Figure 1b. The plasma temperature increased rapidly initially and gradually reached a steady temperature. The temperature was measured by a K-type thermocouple in contact with the substrate.

Sequential screen-printing and APPJ sintering process.— The screen-printing process was performed using a screen-printing machine (WE-400F, Guger Industries Co., Ltd.); the printing-screen has a stencil with a line spacing of 90 μm and net width of 64 μm. The TiO_2 and TiO_2-SnO_2 nanoparticle pastes were prepared according to the procedure described in the literature.[15] Ethyl cellulose (EC) powders, EC (5–15 mPa · s, #46070, Fluka) and EC (30–50 mPa · s, #46080, Fluka), were individually added in ethanol to form two separate 10 wt% ethanolic solutions (hereafter referred to as EC1 (5–15, #46070) and EC2 (30–50, #46080)). 4.5 g of EC1 and 3.5 g of EC2 were added into a round-bottom rotovap flask containing 1.6 g of pure TiO_2 nanoparticles (diameter ~21 nm) and 6.49 g of terpineol (anhydrous, #86480, Fluka). Subsequently, 8 mL of ethanol was added into the rotovap flask for dilution. The mixture was stirred at 450 rpm for 24 h. Finally, the ethanol was removed from this TiO_2/ethyl cellulose mixture using a rotary concentrator operated at 55°C for 1 h. For the TiO_2-SnO_2 composite, the procedure is the same except that 1.4 g TiO_2 and 0.02 g SnO_2 (diameter ~35–55 nm) mixed powders were used instead of pure TiO_2 powders. The flowchart of the preparation procedure of the nanoporous oxides is shown in Figure 2.

Fabrication of thin-film samples.— TiO_2 or TiO_2-SnO_2 nanoparticle pastes were screen-printed onto glass substrates (Corning Eagle 2000) via a 1 cm^2 square grid. The thickness was ~3 μm. APPJ was then used to sinter the printed pastes for various durations. A counterpart thin film sample was fabricated by the same procedure with furnace calcination at 575°C for 1 h instead of APPJ sintering.

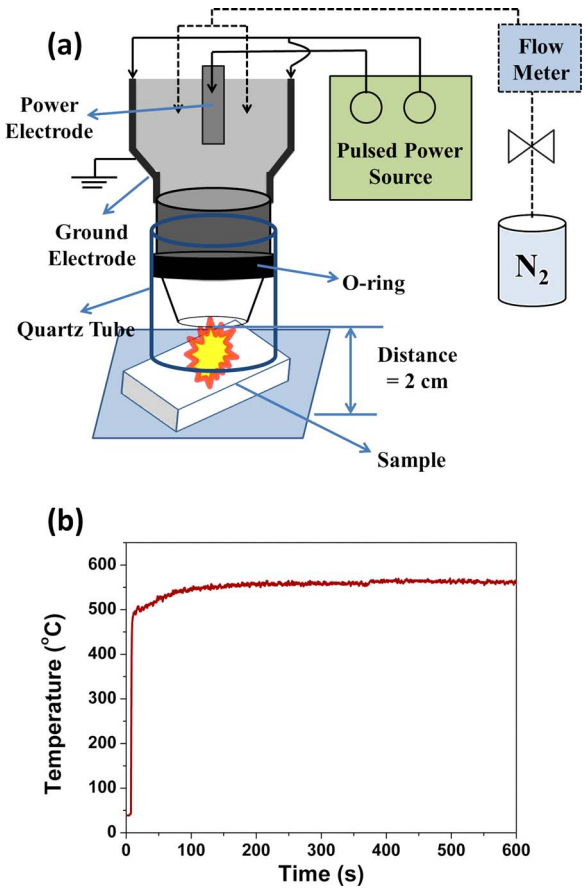

Figure 1. (a) Schematic of APPJ apparatus, and (b) evolution of substrate temperature during APPJ operation.

Fabrication of DSSCs.— TiO_2 or TiO_2-SnO_2 nanoparticle pastes were screen-printed onto a fluorine-doped tin-oxide-coated glass (FTO, TEC7, thickness: 2.2 mm, transmittance: >80%, sheet resistance: 8 Ω/□, Pilkington) with an area of 0.22 cm^2 three times, and the total thickness of the nanoporous TiO_2 layer was ∼10 μm. After each printing step, the printed layer was baked at 100°C for 10 min to partially dry the solvent. Subsequently, APPJ sintering was performed for various durations. The APPJ-sintered TiO_2 and TiO_2-SnO_2 nanoporous films were immersed in a mixed solution of acetonitrile (99.9%, J. T. Baker) and tertiary butyl alcohol (99.9%, J. T. Baker) containing 3×10^{-4} M of N719 dye (Solaronix) for 24 h. The dye-anchored nanoporous oxide photoanodes were rinsed with ethanol, dried at room temperature, and then assembled with the counter electrode of a 10-nm-thick sputtered Pt layer on the FTO glass substrate. Finally, a liquid electrolyte based on the iodide redox in acetonitrile (E-Solar EL 100, Everlight Chemical Industrial Co.) was injected into the assembled cells to complete the assembly of the DSSC. A counterpart DSSC was fabricated by the same procedure with furnace calcination at 500°C for 1 h instead of APPJ sintering.

Characterization of films and DSSCs.— The APPJ-sintered nanoporous oxides were examined by scanning electron microscopy (SEM, Nova NanoSEM 230, FEI) and X-ray diffraction (XRD, PANalytical X'Pert PRO). The specular and total transmittances were measured using a spectrophotometer (JASCO V-670). The transmittance haze values were then calculated based on the transmittance data. It is noted that the resistance of these samples was too high to be measured using an electrometer (Keithley 2636A). To evaluate the DSSC performance, the cells were illuminated through the photoanode side using a solar simulator (Abet Sun 2000 solar simulator class AAB) with an AM1.5 filter. A Keithley 2400 electrometer was used to evaluate the I-V characteristics.

Results and Discussion

Figure 3 shows SEM images of APPJ-sintered TiO_2 and TiO_2-SnO_2 nanoporous composites. A clear nanoporous feature was identified, and some large pores (>80 nm) were formed probably owing to particle agglomeration. No significant alteration of morphology was observed with the increase in APPJ sintering time. Figure 4 shows the XRD patterns of nanoporous oxides. Most diffraction peaks were attributed to the anatase TiO_2 phase. The average grain size d was estimated using the Scherrer equation[23,24] $d = 0.9\,\lambda/B\cos\theta$, where λ, B, and θ are the X-ray wavelength (0.15418 nm for Cu K_α), full-width at half-maximum (FWHM) of the diffraction peak, and Bragg diffraction angle, respectively. The data for the (101) diffraction peak was used to calculate the grain size. The average grain size of APPJ-sintered oxides was ∼20 nm, which was similar to that of the nanoporous oxide obtained by furnace calcination; the grain size remained similar as the APPJ sintering time increased. The calculated grain sizes are listed in Table I.

In this study, the applied APPJ-sintering temperature is ∼500°C, which is considerably lower than that typically used for conventional furnace sintering of an oxide material. We speculate that the application of nano-sized particles may be advantageous in this APPJ-sintering process. Melting point depression (i.e., decrease in melting point temperature) is expected when the particle diameter is reduced. The particle (or pore) size dependent melting temperature can be described based on the classical thermodynamic Gibbs-Thomson relation[25,26]

$$T_M(r) = T_{MB}\left(1 - \frac{4\sigma_{sl}}{H_f \rho_s x}\right) \quad [1]$$

where T_{MB} is the bulk melting temperature; σ_{sl}, the solid-liquid interfacial energy; H_f, the bulk heat of fusion; ρ_s, the density of the solid; and x, the particle or pore size. In practice, the melting point of the semiconductor and covalently bonded nanoparticles may have different dependence on particle size; it is described as[27]

$$T_M(r) = T_{MB}\left(1 - \left(\frac{c}{x}\right)^2\right) \quad [2]$$

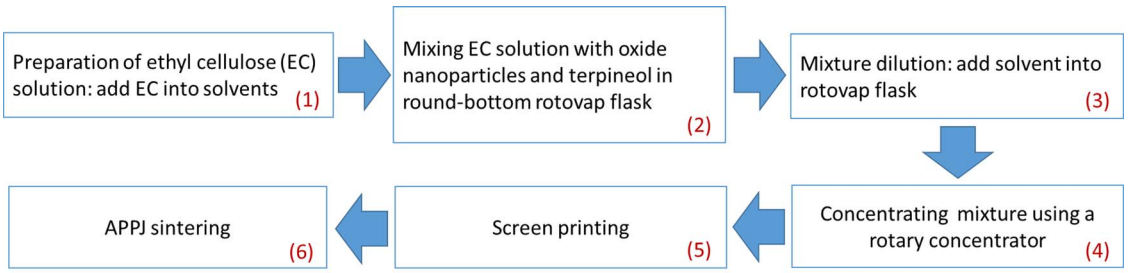

Figure 2. Flow chart of experimental procedure.

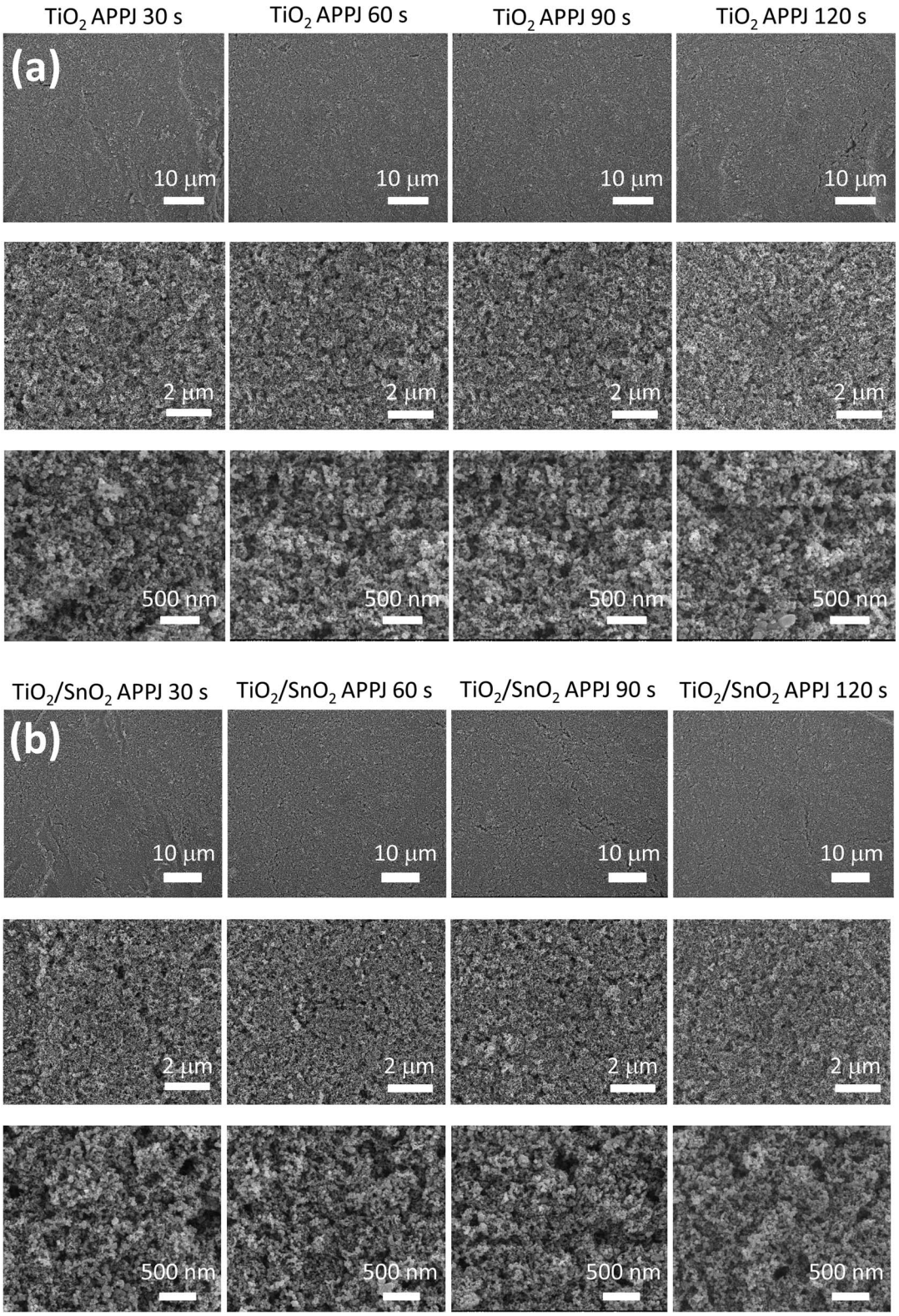

Figure 3. SEM images of APPJ sintered nanoporous (a) TiO_2 and (b) TiO_2-SnO_2 composite.

where c is a material constant. A solid starts to melt when the atomic vibration amplitude reaches a critical fraction (∼10%) of the nearest-neighbor distance. Because of fewer bonds and reduced cohesive energy possessed by the surface atoms, the activity of surface atoms can be much more vibrant than that of bulk atoms, i.e., the melting point of the surface layer is lower than that of the bulk material.[28] Lower melting point usually implies higher activity of mass transport at a certain temperature when no other phase transition or material transformation occurs in a solid. Owing to the large surface-area-to-volume ratio of the nanoparticles, much more vigorous surface mass transport activity is expected for the nanoparticles, which thereby reduces the required sintering temperature.

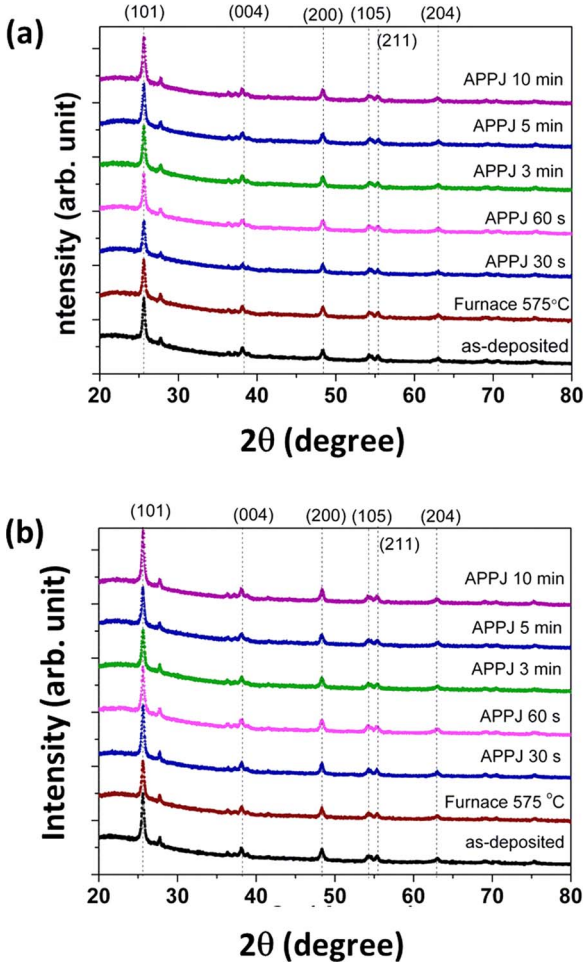

Figure 4. XRD patterns of nanoporous (a) TiO_2 and (b) TiO_2-SnO_2 composite.

The other advantage favoring the APPJ-sintering of nanoparticles is the increase in inter-particle contact area per unit volume as the particle diameter reduces. The surface area is proportional to r^2 and volume is proportional to r^3; therefore, the contact-area/volume ratio scales as 1/r. As the particle radius r decreases, the contact-area/volume ratio increases dramatically. Because of the small-diameter nanoparticles used in this APPJ-sintering process, the large amount of contact points and contact area provide a strong supporting force for the sintered nano-particulate network. Sufficient mechanical strength can be achieved with slight mass transport to bind the nanoparticles effectively.

Figure 5 shows the transmittance haze of sintered nanoporous oxides. The haze values of APPJ sintered oxides were close to that of the nanoporous oxide by conventional furnace calcination. The haze of glass substrate is also plotted as a reference. In both TiO_2 and TiO_2-SnO_2 nanoporous oxides, the haze decreased first and then increased as the APPJ time increased. The initial sintering process smoothens the particulate nature of the nanoporous oxides, further increasing the sintering time may cause cracking or detachment of some particles owing to the unbalance of stresses at the inner and outer layers, causing the increase of haze values. As indicated by the spectra of transmittance haze, 30-s APPJ treatment already showed nearly complete removal of the organic binders. Nitrogen plasmas consist of abundance of N_2 species in the plasma jet. These excited plasma species possess >6 eV higher energy level above the ground state. This highly energetic plasma species may provide extra energy for the removal of the organic compounds.[21,22] Trace level of oxygen from the ambient air may also help the oxidation of the organic binders.[17,29–31] The synergetic effect of heat and highly energetic plasma species leads to this ultrafast removal of the organic binders. This is consistent with the experimental results from our previous study regarding APPJ-sintering on pastes containing rGOs.[19] The required APPJ-sintering time for the rGOs pastes was merely 11 s; nearly all organic compounds including rGOs and ethyl cellulose were removed as the APPJ-sintering

Table I. Grain sizes calculated based on (101) diffraction peaks in Figure 4.

TiO_2 peak (101)	Grain size (nm)
As-deposit	20.46
Furnace anneal@575°C	20.35
APPJ 30 s	20.71
APPJ 60 s	20.60
APPJ 3 min	20.16
APPJ 5 min	20.14
APPJ 10 min	19.54
TiO_2/SnO_2 peak (101)	Grain size (nm)
As-deposit	20.53
Furnace anneal@575°C	20.57
APPJ 30 s	20.24
APPJ 60 s	20.15
APPJ 3 min	20.02
APPJ 5 min	20.41
APPJ 10 min	20.44

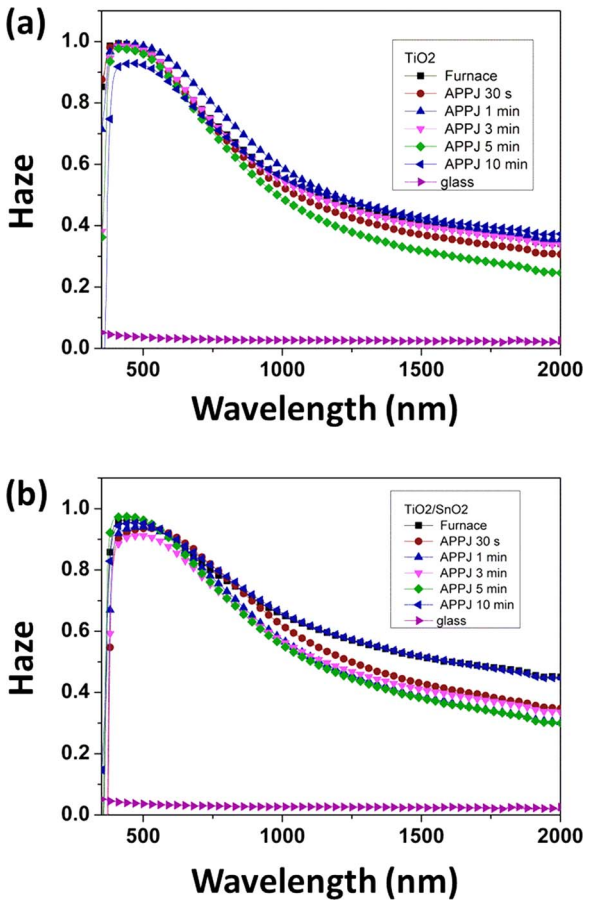

Figure 5. Transmittance hazes of nanoporous (a) TiO_2 and (b) TiO_2-SnO_2 composite.

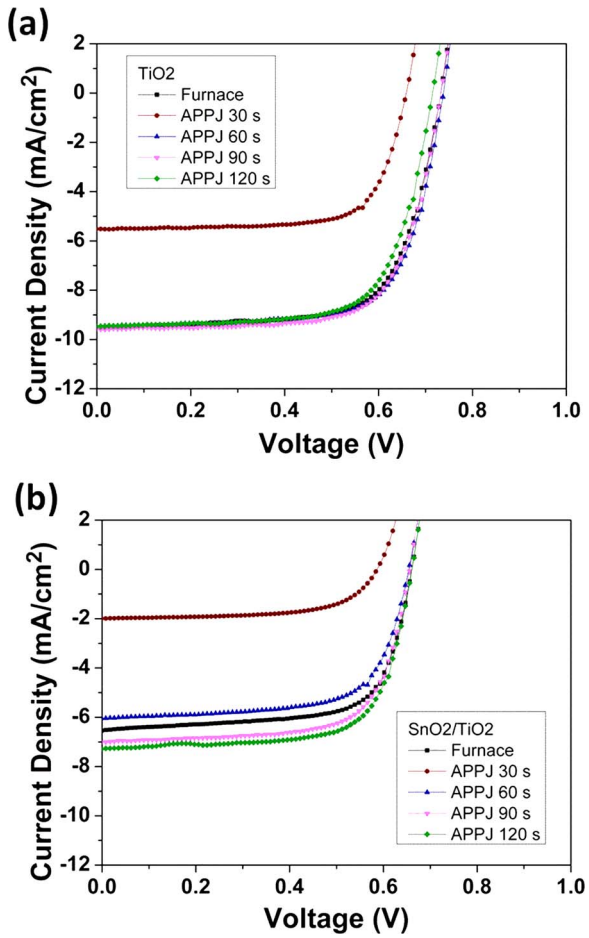

Figure 6. IV curves of DSSCs with nanoporous (a) TiO_2 and (b) TiO_2-SnO_2 composite photoanodes.

increased to 2 min. In contrast, the required calcination time by conventional furnace would take 15 min at 400°C.

The high haze values occur in the wavelength range between 350–700 nm, which could be beneficial for the improvement of light trapping and light scattering for solar cells. Figure 6 shows the J-V curves of DSSCs with TiO_2 and TiO_2-SnO_2 photoanodes; the corresponding cell performance parameters are listed in Table II. For DSSCs with TiO_2 photoanodes (Figure 6a), the DSSC performance became comparable to that of the cell by furnace calcination as the TiO_2 sintering time reached and exceeded 1 min, whereas the DSSC with 30-s APPJ-sintered photoanode showed poor performance. This is consistent with our previous experimental results.[16,17] Figure 6b shows the performance of DSSCs with TiO_2-SnO_2 composite photoanodes. Similar to DSSCs with TiO_2 photoanodes, the cell with a 30-s sintered photoanode showed poor cell performance. The cell efficiency approached that of the DSSC by conventional furnace calcination as the APPJ sintering time reached 1 min. The DSSC efficiency surpassed that of cell by furnace calcination as the sintering time was further increased. These experimental results indicate that 1 min is the minimum time for the complete removal of organic binders for the oxide nanoparticle pastes prepared using the presented procedure (N_2 APPJ without air-quenching), in good agreement with our previous results.[16,17] SnO_2 has much higher electron mobility, comparable bandgap to TiO_2, and 0.3 eV more negative conduction band minimum than that of TiO_2. These factors benefit the electron injection from the excited dyes into the photoanodes and the electron transport in the photoanodes when TiO_2-SnO_2 composite instead of bare TiO_2 is used; therefore, higher efficiency is expected. However, the experimental results showed that the efficiency of DSSCs deteriorated as SnO_2 was added into TiO_2. This could be due to the relatively weak adsorption of the dyes with acidic anchoring groups to the SnO_2, and the recombination of conduction band electrons with the oxidized dyes.[32] The lower photocurrent levels for the DSSCs with TiO_2-SnO_2 photoanodes support this inference. The larger particle size of SnO_2 also reduced the surface-area to volume ratio, leading to the decreased total area for the anchoring of dyes when SnO_2 powders were mixed into TiO_2 ones. With the addition of SnO_2, the cells possessed lower open circuit voltages. Generally the open circuit voltage roughly corresponds to the difference of the conduction band level of the oxide photoanode and the redox potential level.[33] The lower conduction band minimum of SnO_2 could lead to the decreased open circuit voltage when the same electrolyte redox pair is used.

Table II. DSSC performance parameters.

TiO_2	J_{SC} (mA/cm^2)	V_{OC} (V)	FF (%)	Efficiency (%)
Furnace	9.51	0.73	69.9	4.84
APPJ 30 s	5.51	0.66	72.8	2.63
APPJ 60 s	9.48	0.74	70.4	4.92
APPJ 90 s	9.56	0.73	69.8	4.93
APPJ 120 s	9.47	0.72	69.1	4.71
TiO_2-SnO_2	J_{SC} (mA/cm^2)	V_{OC} (V)	FF (%)	Efficiency (%)
Furnace	6.55	0.66	68.9	2.96
APPJ 30 s	1.99	0.58	63.2	0.74
APPJ 60 s	6.04	0.66	67.3	2.66
APPJ 90 s	7.00	0.66	69.1	3.17
APPJ 120 s	7.29	0.67	68.9	3.34

Conclusions

We successfully fabricated nanoporous TiO_2 and TiO_2-SnO_2 materials using a two-step process consisting a sequential screen-printing and APPJ-sintering processes. Highly reactive species in N_2 plasmas and heat can efficiently remove organic binders in the pastes and sinter the oxide nanoparticles in 30 s; the sintered oxides showed transmittance haze values comparable to those of nanoporous oxides prepared by furnace calcination. 1 min APPJ sintering affords more complete removal of the organic binders; therefore, the DSSCs with 1-min APPJ-sintered photoanodes show comparable efficiency to those of cells prepared by the conventional furnace calcination. This rapid nanoporous oxides synthesis technique can be applied to the fabrication of gas sensors, catalysts, batteries, and supercapacitors, in which the active materials with high surface-area to volume ratio are essential for an improved device performance.

Acknowledgments

This work is supported by the Ministry of Science and Technology of Taiwan under grand no. MOST 103-2221-E-002-057. ICC and JZC are currently visiting research scholars at Princeton University, New Jersey, USA. The visits are supported by the Ministry of Science and Technology of Taiwan under grand nos. MOST 103-2918-I-002-005 (JZC) and MOST 103-2918-I-002-004 (ICC).

References

1. H.-B. Lee, H. Yang, J. We, K. Kim, K. Choi, and B. Cho, *Journal of Electronic Materials* **40**(5), 615 (2011).
2. S. Ito, P. Chen, P. Comte, M. K. Nazeeruddin, P. Liska, P. Pechy, and M. Gratzel, *Prog Photovoltaics* **15**(7), 603 (2007).
3. Y. F. Xu, M. G. Schwab, A. J. Strudwick, I. Hennig, X. L. Feng, Z. S. Wu, and K. Mullen, *Adv Energy Mater* **3**(8), 1035 (2013).
4. K. Y. Xie and B. Q. Wei, *Adv Mater* **26**(22), 3592 (2014).
5. A. S. Garde, *J Alloy Compd* **617**, 367 (2014).
6. T. Nomura, T. Maeda, and T. Wada, *Jpn J Appl Phys* **53**(5), 05FW01 (2014).

7. R. Zichner and R. R. Baumann, *Jpn J Appl Phys* **52**(5), 05DC24 (2013).
8. X. L. Yu, C. S. Xie, L. Yang, and S. P. Zhang, *Sensor Actuat B-Chem* **195**, 439 (2014).
9. X. Lin, H. Subbaraman, Z. Pan, A. Hosseini, C. Longe, K. Kubena, P. Schleicher, P. Foster, S. Brickey, and R. T. Chen, *Electronics* **3**, 624 (2014).
10. X. Cao, H. Chen, X. Gu, B. Liu, W. Wang, Y. Cao, F. Wu, and C. Zhou, *Nano Letters*, (2014).
11. Z. N. Bao, Y. Feng, A. Dodabalapur, V. R. Raju, and A. J. Lovinger, *Chem Mater* **9**(6), 1299 (1997).
12. E. Menard, M. A. Meitl, Y. G. Sun, J. U. Park, D. J. L. Shir, Y. S. Nam, S. Jeon, and J. A. Rogers, *Chem Rev* **107**(4), 1117 (2007).
13. G. S. Ryu, J. S. Kim, S. H. Jeong, and C. K. Song, *Org Electron* **14**(4), 1218 (2013).
14. T. Sekitani, H. Nakajima, H. Maeda, T. Fukushima, T. Aida, K. Hata, and T. Someya, *Nat Mater* **8**(6), 494 (2009).
15. S. Ito, T. N. Murakami, P. Comte, P. Liska, C. Grätzel, M. K. Nazeeruddin, and M. Grätzel, *Thin Solid Films* **516**(14), 4613 (2008).
16. H. Chang, Y. J. Yang, H. C. Li, C. C. Hsu, I. C. Cheng, and J. Z. Chen, *Journal of Power Sources* **234**, 16 (2013).
17. H. Chang, C. M. Hsu, P. K. Kao, Y. J. Yang, C. C. Hsu, I. C. Cheng, and J. Z. Chen, *Journal of Power Sources* **251**, 215 (2014).
18. H. Chang, Y. J. Yang, C. M. Hsu, C. C. Hsu, I. C. Cheng, and J. Z. Chen, *ECS Journal of Solid State Science and Technology* **3**(10), Q177 (2014).
19. H. W. Liu, S. P. Liang, T. J. Wu, H. Chang, P. K. Kao, C. C. Hsu, J. Z. Chen, P. T. Chou, and I. C. Cheng, *ACS Applied Materials and Interfaces* **6**, 15105 (2014).
20. H. H. Huang, H. Chang, H. W. Liu, C. W. Hsu, I. C. Chiu, M. Y. Teng, H. J. Lai, I. C. Cheng, and J. Z. Chen, *Materials Research Express* **1**, 025505 (2014).
21. A. N. Wright and C. A. Wrinkler, *Active Nigrogen*. (Academic Press Inc., New York, 1968).
22. Y.-w. Hsu, Y.-j. Yang, C.-y. Wu, and C.-c. Hsu, *Plasma Chemistry and Plasma Processing* **30**(3), 363 (2010).
23. P. Scherrer, *Nachr. Gottingen* **2**, 98 (1918).
24. A. L. Patterson, *Phys Rev* **56**(10), 978 (1939).
25. J. Sun and S. L. Simon, *Thermochim Acta* **463**(1), 32 (2007).
26. C. L. Jackson and G. B. Mckenna, *J Chem Phys* **93**(12), 9002 (1990).
27. H. H. Farrell and C. D. Van Siclen, *J Vac Sci Technol B* **25**(4), 1441 (2007).
28. J. W. M. Frenken and J. F. Vanderveen, *Phys Rev Lett* **54**(2), 134 (1985).
29. W. Y. Liao, H. M. Chang, Y. J. Yang, C. C. Hsu, I. C. Cheng, and J. Z. Chen, *Appl Surf Sci* **292**, 213 (2014).
30. H. Jung, J. Park, E. S. Yoo, G. S. Han, H. S. Jung, M. J. Ko, S. Park, and W. Choe, *Nanoscale* **5**(17), 7825 (2013).
31. M.-H. Chiang, K.-C. Liao, I.-M. Lin, C.-C. Lu, H.-Y. Huang, C.-L. Kuo, J.-S. Wu, C.-C. Hsu, and S.-H. Chen, *Plasma Chemistry and Plasma Processing* **30**(5), 553 (2010).
32. H. K. Wang and A. L. Rogach, *Chem Mater* **26**(1), 123 (2014).
33. B. E. Hardin, H. J. Snaith, and M. D. McGehee, *Nat Photonics* **6**(3), 162 (2012).